Electronic Supplementary Information for:

Vibrational characterization of a diiron bridging hydride complex – a model for hydrogen catalysis

Leland B. Gee,[‡a] Vladimir Pelmenschikov,[‡*b] Hongxin Wang,[‡c] Nakul Mishra,[d] Yu-Chiao Liu,[e] Yoshitaka Yoda,[f] Kenji Tamasaku,[g] Ming-Hsi Chiang,[*e] and Stephen P. Cramer*[c]

[a] *Department of Chemistry, Stanford University, 333 Campus Drive, Stanford, CA 94305, USA*
[b] *Institut für Chemie, Technische Universität Berlin, Strasse des 17 Juni 135, 10623 Berlin, Germany*
[c] *SETI Institute, 189 Bernardo Avenue, Mountain View, CA 94043, USA*
[d] *Department of Chemistry, University of California, Davis, One Shields Ave, Davis, CA 95616, USA*
[e] *Institute of Chemistry, Academia Sinica, Nankang, Taipei 115, Taiwan and Department of Medicinal and Applied Chemistry, Kaohsiung Medical University, Kaohsiung 807, Taiwan*
[f] *Japan Synchrotron Radiation Research Institute (JASRI), SPring-8, 1-1-1 Kouto, Sayo, Hyogo 679-5198, Japan*
[g] *RIKEN SPring-8 Center, 1-1-1 Kouto, Sayo, Hyogo 679-5148, Japan*

‡ These authors contributed equally.
* Corresponding author.

Materials and Methods

Synthesis

All reactions were carried out by using standard Schlenk and vacuum-line techniques under an atmosphere of purified nitrogen. All commercially available chemicals from Aldrich were of ACS grade and used without further purification. Solvents were of HPLC grade and purified as follows: hexane, diethyl ether and tetrahydrofuran were distilled from sodium/benzophenone under N_2. Dichloromethane was distilled from CaH_2 under N_2. Acetone was distilled over 3 Å molecular sieves under N_2. Deuterated solvents obtained from Merck were distilled over 4 Å molecular sieves under N_2 prior to use. Infrared spectra were recorded on a PerkinElmer Spectrum One instrument using a 0.05 mm CaF cell. ^{1}H, ^{2}H, ^{13}C{^{1}H}, and ^{31}P{^{1}H} NMR spectra were recorded on a Bruker AV-500 or DRX-500 spectrometer operating at 500, 125.7, and 202.49 MHz, respectively. Mass spectral analyses were done on a Waters LCT Premier XE instrument at the Mass Spectrometry Center of the Institute of Chemistry, Academia Sinica. [(μ,κ^2-bdt)(μ-PPh_2)$^{57}Fe_2(CO)_5$]$^-$ was prepared by the literature methods,[4] from [(μ-bdt)$^{57}Fe_2(CO)_6$],[5] then treatment by strong acid afforded [(μ,κ^2-bdtH)(μ-PPh_2)(μ-H)$^{57}Fe_2(CO)_5$]$^+$ (denoted **μHSH**).[6] The perdeuteride derivative was prepared by similar procedures under deuterated solvents to afford [(μ,κ^2-bdtD)(μ-PPh_2)(μ-D)$^{57}Fe_2(CO)_5$]$^+$ (denoted **μDSD**). [(μ,κ^2-bdtCH_3)(μ-PPh_2)$^{57}Fe_2(CO)_5$]$^-$ was prepared from a reaction of [(μ,κ^2-bdt)(μ-PPh_2)$^{57}Fe_2(CO)_5$]$^-$ with CH_3I (4 equiv.) in THF solution, as described in the literature.[7] The subsequent reaction with HCl (2 M in diethyl ether, 3 equiv) and $NaBArF_{24}$ (1 equiv) in CH_2Cl_2 solution afforded [(μ,κ^2-bdtCH_3)(μ-PPh_2)(μ-H)$^{57}Fe_2(CO)_5$]$^+$ (denoted **μHSMe**). The solution was filtered through Celite and the filtrate was concentrated in vacuo. The product was precipitated upon addition of hexane. The yield of **μHSMe** was 35 %. The perdeuteride derivative was prepared by similar procedures with deuterated reagents under deuterated solvents to afford [(μ,κ^2-bdtCH_3)(μ-PPh_2)(μ-D)$^{57}Fe_2(CO)_5$]$^+$ (denoted **μDSMe**). For **μHSMe**: IR (CH_2Cl_2, cm^{-1}): ν_{CO} = 2101 (m), 2057(s), 2043 (m, sh), 2016 (m). ^{1}H NMR (500.13 MHz, $CDCl_3$, 298 K): $\delta = -15.99$ (d, 1H, J^2_{PH} = 48.5 Hz, Fe-*H*-Fe), 2.97 (s, 3H, SCH_3), 7.17-7.78 (m, 26H, $S_2C_6H_4$, P(C_6H_5)$_2$, B(3,5-$C_6H_3(CF_3)_2$)$_4$) ppm. ^{13}C{^{1}H} NMR (125.77 MHz, $CDCl_3$, 298 K): $\delta = 30.76$ (s, 1C, S*C*H$_3$), 127.56 (d, J^2_{PC} = 38.9 Hz, 1C, *ipso*-P(C_6H_5)$_2$), 129.66 (s, 2C), 129.76 (s, 2C), 129.84 (s, 2C), 129.92 (s, 2C), 131.42 (s, 2C), 131.67 (s, 2C), 132.6 (s, 2C), 132.80 (s, 2C), 132.88 (s, 2C), 133.07 (s, 2C), 133.19 (s, 2C), 133.43 (s, 2C), 134.14 (s, 1C), 134.45 (s, 2C), 134.51 (s, 2C), 135.57 (s, 3C, $S_2C_6H_4$, P(C_6H_5)$_2$, B(3,5-C_6H_3(*C*F$_3$)$_2$)$_4$), 137.48 (s, br, 3C), 137.61 (s, 3C), 139.40 (m, br, 2C, *ipso*-$S_2C_6H_4$, *ipso*-B(3,5-C_6H_3(*C*F$_3$)$_2$)$_4$), 140.37 (d, J^2_{PC} = 20.4 Hz, 1C, *ipso*-P(C_6H_5)$_2$), 147.50 (s, 3C), 149.42 (s, 3C, *ipso*-$S_2C_6H_4$, *ipso*-B(3,5-C_6H_3(*C*F$_3$)$_2$)$_4$), 199.23 (d, J^2_{PC} = 24.0 Hz, 1C, *C*O), 203.31 (d, J^2_{PC} = 15.9 Hz, 1C, *C*O), 203.96 (d, J^2_{PC} = 13.7 Hz, 1C, *C*O), 206.35 (d, J^2_{PC} = 15.0 Hz, 1C, *C*O), 207.16 (d, J^2_{PC} = 15.6 Hz, 1C, *C*O) ppm. ^{31}P{^{1}H} NMR (202.46 MHz, $CDCl_3$, 298 K): $\delta = 146.20$ (s) ppm. ESI MS(+ mode)：m/z 595.0 {**M**}$^+$, 567.0 {**M**–CO}$^+$, 539.0 {**M**–2CO}$^+$, 511.0 {**M**–3CO}$^+$, 483.0 {**M**–4CO}$^+$, 455.0 {**M**–5CO}$^+$, 440.0 {**M**–5CO–CH_3}$^+$.For **μDSMe**: IR (CH_2Cl_2, cm^{-1}): ν_{CO} = 2101 (m), 2057(s), 2043 (m, sh), 2016 (m). ^{2}H NMR (76.77 MHz, CH_2Cl_2, 298 K): $\delta = -16.08$ (d, 1D, J^2_{PD} = 7.2 Hz, Fe-*D*-Fe) ppm. ^{31}P{^{1}H} NMR (202.46 MHz, CH_2Cl_2, 298.4 K): $\delta = 146.34$ (s) ppm. ESI MS(+ mode): m/z 596.0 {**M**}$^+$, 568.0 {**M**–CO}$^+$, 540.0 {**M**–2CO}$^+$, 512.0 {**M**–3CO}$^+$, 484.0 {**M**–4CO}$^+$, 456.0 {**M**–5CO}$^+$, 441.0 {**M**–5CO–CH_3}$^+$.

^{57}Fe NRVS

^{57}Fe NRVS was collected at the synchrotron radiation facility SPring-8 at BL09XUand BL19LXU with different samples measured during the 2015A, 2016A, 2016B, 2018A, and 2018B beamtime periods. The storage ring was operating in the C-mode bunch pattern (with a 145 ns interval between X-ray pulses).[8] The samples were placed in a helium flow cold finger cryostat maintained at 10 K but the samples' true temperatures ranged from 45-60 K determined by the "detailed balance" method within the PHOENIX analysis. The X-ray beams from the planar undulators were monochromatized by high heat load monochromators to ≈1 eV bandwidth, and then further monochromatized by a Ge(331)x2Si(975) high resolution monochromator (HRM) to 0.8 meV linewidth centered at the nuclear resonance energy of ^{57}Fe (14.4 keV). The final beam flux at BL09XU was 1.4×10^9 photon s^{-1} and that at BL19LXU was 4x10^9 photon s^{-1} (both at the time of the measurements). A 2×2 avalanche photodiode (APD) array detector was used to detect the ^{57}Fe nuclear fluorescence and the Fe K fluorescence from internal conversion following the nuclear resonance excitation. As the nuclear scattering process has a much longer relaxation time than the electron scattering processes, the strong electron scattering from the prompt pulse was filtered out from the weak NRVS signal by using time-resolved Si APD detectors and time-electronics synchronized with the synchrotron bunch clock. Spectral processing was performed with PHOENIX executed through spectra.tools to yield ^{57}Fe partial vibrational density of states (PVDOS).[9, 10] In order to calculate PVDOS, the Fourier-log method[11] and spectral normalization through Lipkin's sum rule were used.[12] Region-of-interest scans were utilized for energies >800 cm^{-1} to ensure the error of the final data remained similar throughout this region.

^{57}Fe Mössbauer spectroscopy

The ^{57}Fe Mössbauer spectrum of **μHSH** was collected using a SEE Co. W202 gamma-ray spectrometer operating with a Janis SVT400 high efficiency LHe/LN2 cryostat using ^{57}Co in a rhodium matrix as the gamma-ray source. The sample was held nominally at 80 K with liquid nitrogen. Isomer shifts quoted relative to α-Fe foil at 298 K. Fits of quadrupole doublets to the obtained spectrum were conducted with the MossWinn software.[13]

DFT

Crystallographic CCDC 913856 data[14] has been used to generate starting structures for the present DFT models **μHSH**, **μHSH$_{in}$**, **μHS$^-$**, and **[μHSH]$_2$** (Fig. S3). The **μHSMe$_{in}$** methylated species model was based on the **μHSMe$_{in}$(OMe)$_2$** species X-ray structure (results unpublished), with the two –OMe groups initially substituted by protons (Fig. S4). The structure optimization and subsequent normal mode analysis were done using GAUSSIAN 09,[15] based on the densities exported from single point calculations using JAGUAR 9.4.[16] The BP86[17, 18] functional and the LACV3P** basis set were employed. For the first- and second-row elements, LACV3P** implies 6-311G** triple-zeta basis sets including polarization functions. For the Fe atoms, LACV3P** consists of a triple-zeta quality basis set for the outermost core and valence orbitals, and the quasirelativistic Los Alamos effective core potential (ECP) for the innermost electrons.[19, 20] The model environment was considered using a self-consistent reaction field (SCRF) polarizable continuum model and integral equation formalism (IEF-PCM) as implemented in GAUSSIAN 09, with IEF-PCM parameters at their default values for liquid water. Based on the normal mode outputs from GAUSSIAN 09, an in-house Q-SPECTOR program successfully applied previously (*e.g.* in refs.[21-23]), was utilized to generate the partial vibrational density of states (PVDOS) for the ^{57}Fe and hydride-specific (H^-/D^-) nuclei from the normal mode composition factors. Additionally, to the computational details provided above, the calculations on the **[μHSH]$_2$** dimer model included the two-body D3 dispersion corrections by Grimme et al.[24, 25] as implemented in GAUSSIAN 09. A homogeneous empirical scaling of the calculated frequencies by 104% <400 cm^{-1} and by 98% >400 cm^{-1} has been uniformly applied to all the DFT model frequencies in order to improve matching to the observed NRVS bands. The resolution of the observed NRVS spectra was accounted for by convolution of the computed PVDOS intensities with a full width at half maximum (FWHM) = 12 cm^{-1} Lorentzian. Vector (arrow-style) and animated representations of the normal modes in the model molecular frameworks were generated using ChemCraft.[26]

^{57}Fe Mössbauer isomer shift and quadrupole splittings DFT calculations were conducted with the Orca software version 4.0.0,[27] after reoptimization using the B3LYP[28-31] functional, and 6-311G basis set without a solvation model to properly apply the isomer shift calibration constants from Mulder et al.[32]

Supplementary Discussion

The diiron core electronic structure from ^{57}Fe Mössbauer spectroscopy and DFT calculations

The ^{57}Fe Mössbauer spectrum of the **μHSH** complex (Fig. S2) is best fit by two quadrupole doublets. The isomer shift and quadrupole splitting of the first doublet are 0.098 and 0.620 mm/s respectively. The second doublet features an isomer shift of -0.047 and quadrupole splitting of 0.695 mm/s. We also fit a, likely ferrous impurity, doublet that comprises 7% of the overall spectrum.

The Mössbauer spectrum isomer shift values for the two $Fe_{d/p}$ sites are low. It has been demonstrated previously for similar diiron complexes, that isomer shift is a better metric for ligation rather than direct oxidation.[33] The very low isomer shift in similar diiron complexes can be partially attributed to π-acceptor/σ-donor ligands as expected of the terminal carbonyls.[34] Also, the bridging H^- donates electron density into the 4*s* orbitals of the Fe atoms and drives the isomer shift to lower values; although perhaps intuitive, the effect has been observed previously with a terminal hydride intermediate in [FeFe] hydrogenase,[32] a bridging hydride in a [NiFe] hydrogenase model complex,[35] and in a terminal hydride phosphine complex.[36] The doublet with the higher isomer shift is reasonably identified as the proximal Fe_p site (see Fig. S1a for atomic labels) as it has one less carbonyl and instead a protonated thiol that lowers the *s*-electron density at the iron and correspondingly increases the isomer shift relative to the distal Fe_d, with both transition metals in the formally low spin Fe(II) state.

The intuition is supported by our DFT-predicted values for isomer shift on each iron. Utilizing the B3LYP functional and the calibration by Mulder et al.,[32] the calculated isomer shift values are 0.097 mm/s for Fe_p and -0.043 mm/s for Fe_d with quadrupole splittings of -0.826 and 0.908 mm/s respectively. Although we note that global DFT hybrid functionals perform poorly compared to range-separated functionals in the calculations of electric field gradients (and thus quadrupole splittings)[37] – we implemented the B3LYP functional as a convenience, as there are existing isomer shift calibrations for B3LYP on similar diiron complexes[32] and considered isomer shift as a more important observable to distinguish the two irons in this case. As indicated by the above values, we find that the approach and calibration constants by Mulder et al.[32] performed exceptionally well for predicting the **μHSH** isomer shift. Other methods and calibration constants for isomer shift did not reproduce the experimental results so well[38] – and is possibly a result of the dissimilarity of **μHSH** with the molecules in test sets used to generate the other calibrations.

Table S1 Fe–Fe/H/S_p internuclear distances (Å) involving two iron sites and bridging hydride from the X-ray structural reference **[μHSH]$_2$** and DFT-optimized models **[μHSH]$_2$**, **μHSH**, **μHSH$_{in}$**, **μHS$^-$** and **μHSMe$_{in}$** shown in Figs. S3 and S4. The atomic Fe labels used are as specified in Fig. S1a. For the **[μHSH]$_2$** dimer, distances in two clustered enantiomers **μHSH** and **μHSH$_m$** are provided separately.

	X-ray		**DFT**					
	[μHSH]$_2$		**[μHSH]$_2$**		**μHSH**	**μHSH$_{in}$**	**μHSMe$_{in}$**	**μHS$^-$**
	μHSH	**μHSH$_m$**	**μHSH**	**μHSH$_m$**				
Fe$_p$–Fe$_d$	2.61	2.61	2.618	2.616	2.622	2.624	2.628	2.650
Fe$_p$–H	1.71*	1.61*	1.719	1.724	1.731	1.725	1.725	1.770
Fe$_d$–H	1.60*	1.68*	1.662	1.659	1.651	1.650	1.654	1.630
Fe$_p$–S$_p$	2.30	2.29	2.326	2.331	2.331	2.329	2.323	2.319

* The experimental Fe–H distances are expected to suffer from inaccuracies, as known from X-ray crystallography studies.[39]

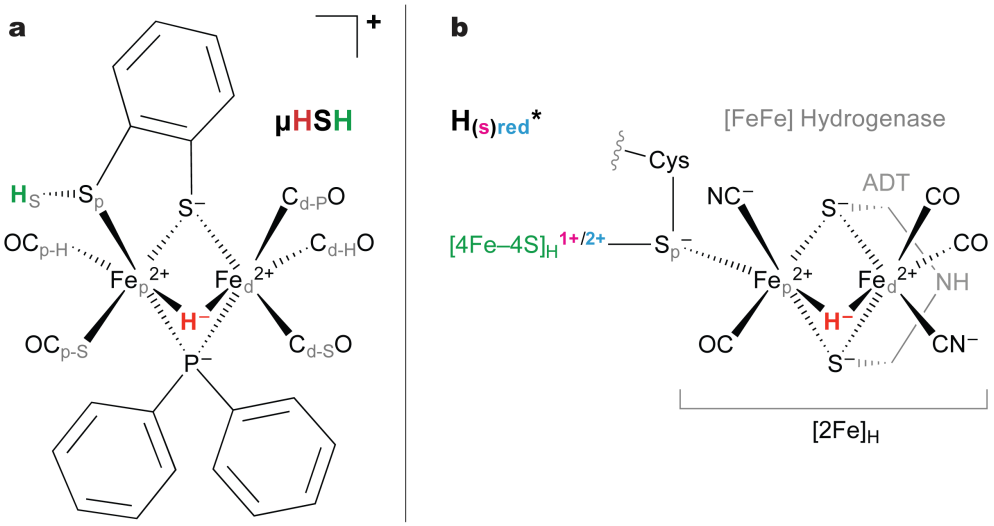

Fig. S1 Schematic structural parallels between (**a**) the main species **μHSH** of this study and (**b**) H-cluster of [FeFe] hydrogenase in its proposed[1-3] variant of intermediate H(s)red. In (**b**), $[2Fe]_H$ and $[4Fe\text{-}4S]_H$ sub-clusters are shown bridged by the protein cysteine thiolate, and azadithiolate (ADT) ligand is in the background. The * sign implies the nature of H(s)red under debate. The bridging (μ)H^- hydride is shown in red.

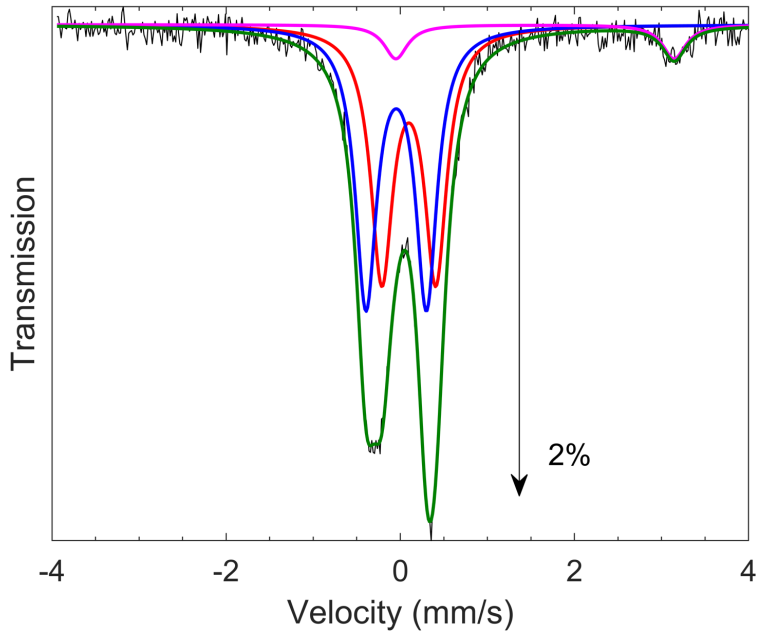

Fig. S2 ^{57}Fe Mössbauer spectrum of **μHSH** with two primary features corresponding to the two iron sites $Fe_{d/p}$, and a single quadrupole doublet of a (7%) ferrous impurity.

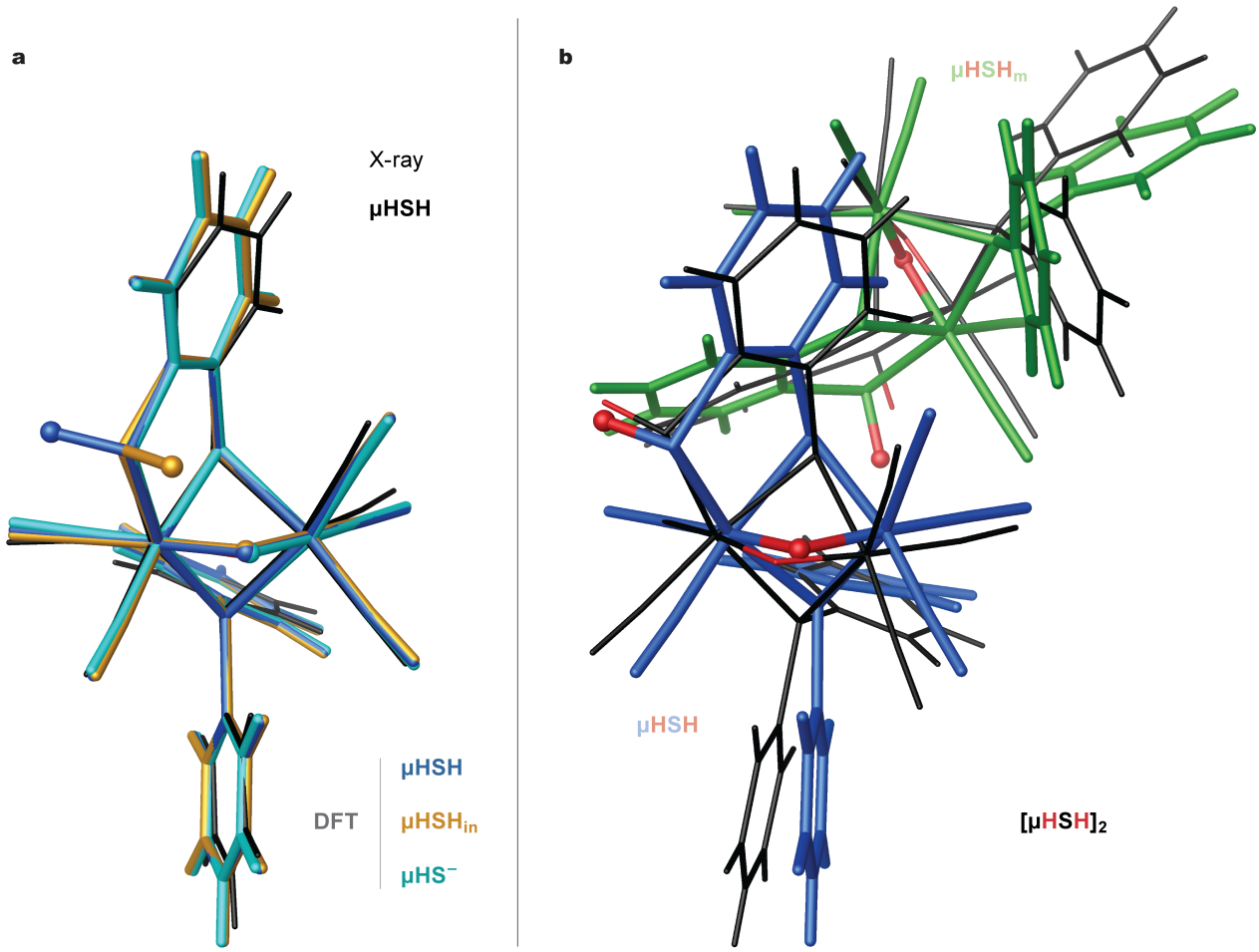

Fig. S3 DFT-optimized model alternatives for species **µHSH** employed in this study: (**a**) **µHSH** (blue), **µHSH$_{in}$** (beige), and **µHS$^-$** (cyan) monomers and (**b**) dimer **[µHSH]$_2$** composed from enantiomers **µHSH** (blue) and **µHSH$_m$** (green). The X-ray reference and DFT-optimized structures are shown overlaid in wire (black) and tube (model-specific colors) representations, respectively. The exchangeable protons are additionally shown in ball representation.

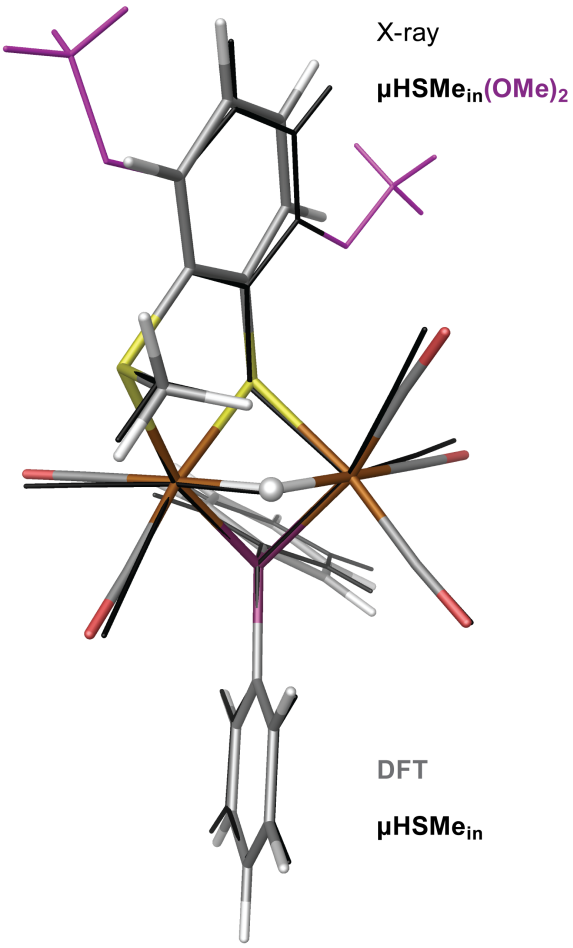

Fig. S4 DFT-optimized model for species **μHSMe** employed in this study. The **μHSMe$_{in}$(OMe)$_2$** variant X-ray reference and DFT-optimized **μHSMe$_{in}$** structures are shown overlaid in wire (black) and tube (element-specific colors) representations, respectively. The exchangeable protons are additionally shown in ball representation. The two –OMe groups of **μHSMe$_{in}$(OMe)$_2$**, altered to protons in the **μHSMe$_{in}$** model, are shown in purple.

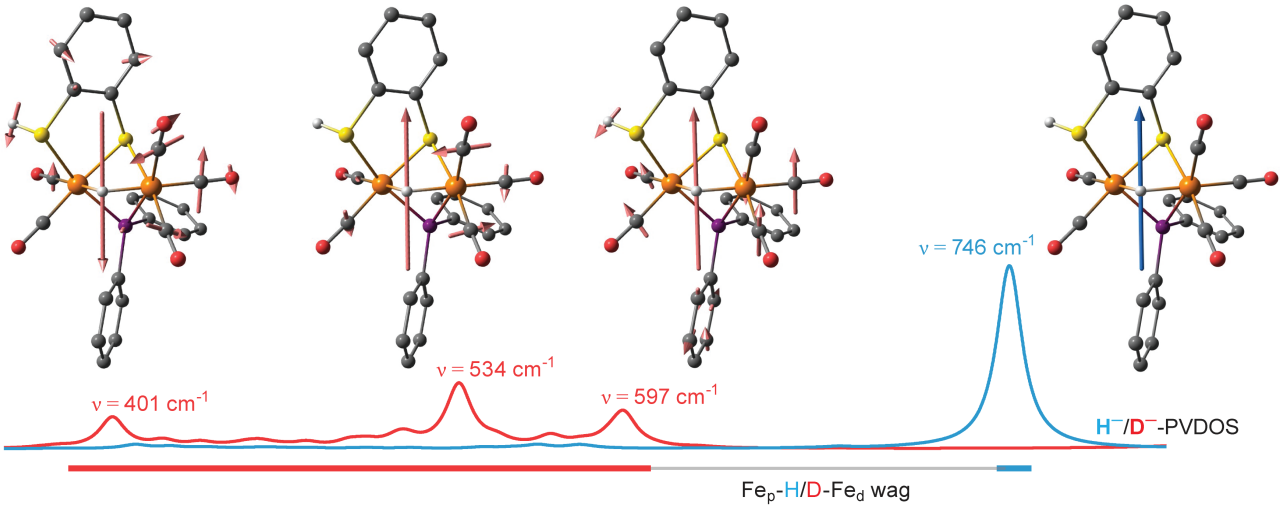

Fig. S5 Arrow-style representation of the calculated wagging hydride vibrational modes in **μHSH** (right), and its isotopologue **μDSD** (left), together with the corresponding ~400-800 cm^{-1} section of the H^-/D^--PVDOS (Fig. S7d). Actual H^-/D^- nuclei displacements in the modes depicted are respectively ~0.2/0.1 Å. The H/D-variant data are respectively in blue/red. Only the two H/D exchangeable protons are shown for clarity. Animated representations of these vibrational modes are available in ESI† separately.

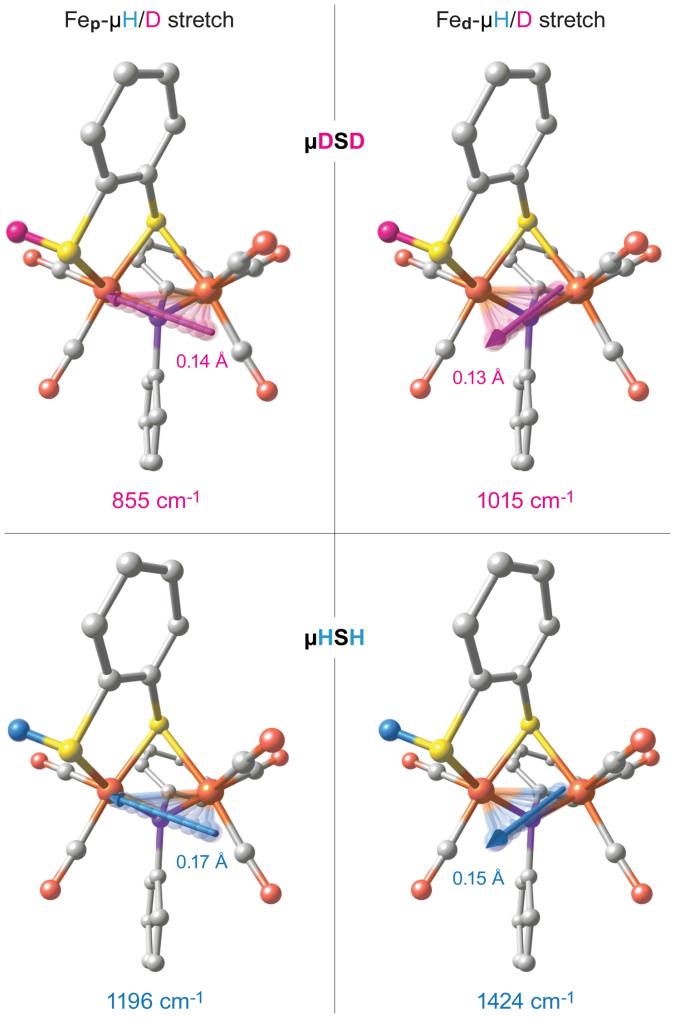

Fig. S6 Pseudo-dynamic (amplitudes exaggerated) and arrow-style representations of the stretching iron-hydride vibrational modes Fe_p-μH/D (left) and Fe_d-μH/D (right) from DFT models **μHSH** (bottom) and its isotopologue **μDSD** (top). Only the two H/D exchangeable protons are shown for clarity, correspondingly in blue/magenta. Actual H^-/D^- nuclei displacements in the modes depicted are additionally provided (Å). Animated representations of these vibrational modes are available in ESI† separately.

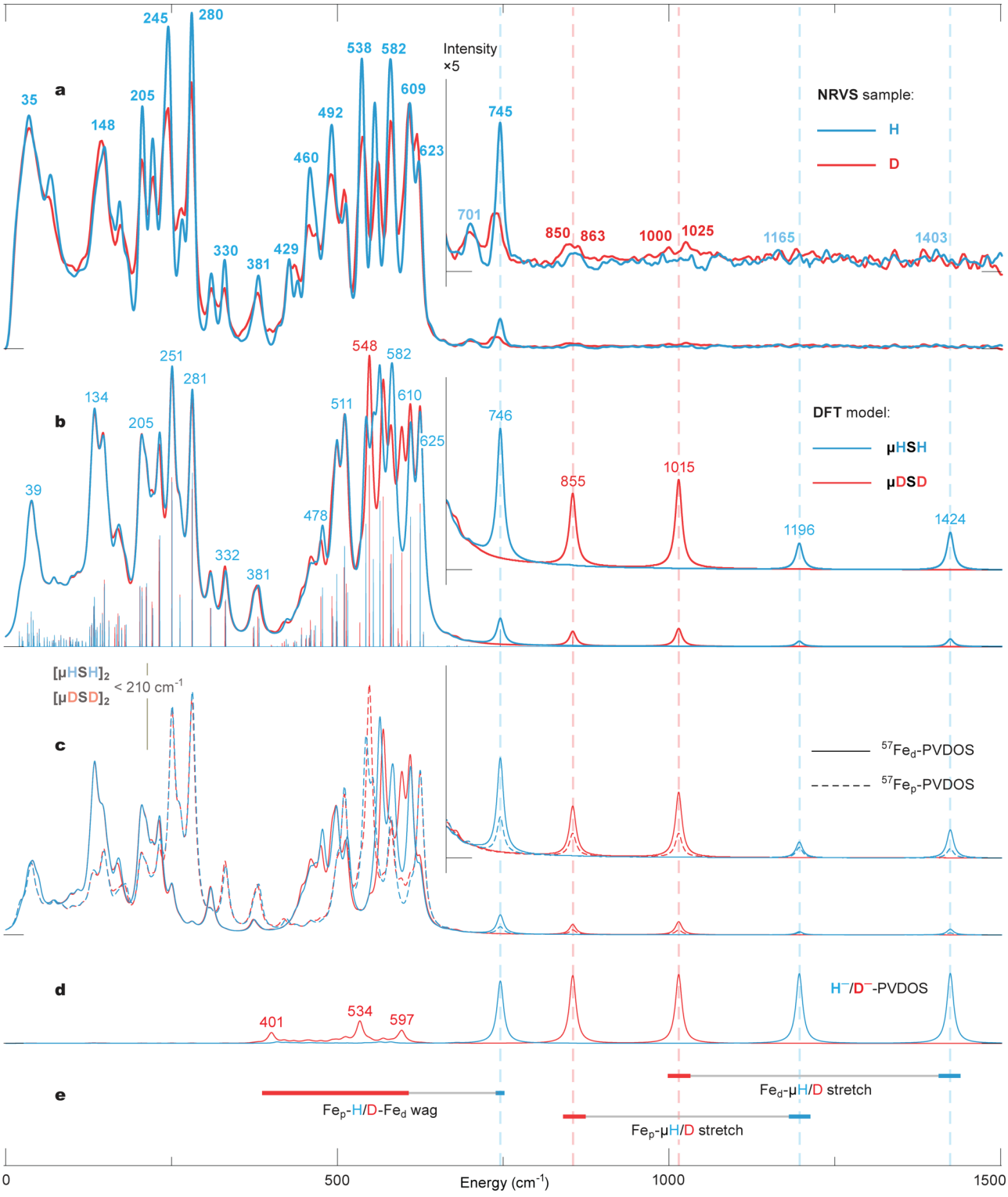

Fig. S7 ^{57}Fe-PVDOS spectra for the H- (**μHSH**, blue) and D-isotopologues (**μDSD**, red) from (**a**) NRVS experiments and (**b**) DFT calculations, followed by DFT-based (**c**) individual contributions to ^{57}Fe-PVDOS from sites Fe_d and Fe_p, and (**d**) H^-/D^--PVDOS from the bridging hydride/deuteride nuclei. The hydride-dependent bands and their H^--to-D^- shifts are indicated in (**e**). The ×5 intensity insets in (**a**-**c**) display the 'active window' ^{57}Fe-hydride bands region >650 cm^{-1}, where equivalences between the observed and computed features are indicated by broken vertical lines. In (**a**), the NRVS bands assignment >800 cm^{-1} is tentative. The DFT intensities <210 cm^{-1} are based on the **[μHSH]$_2$** dimer calculations, as explained in the main text and shown in Fig. 5. For the effects explaining Fe-μH/D NRVS bands dispersion >800 cm^{-1} in (**a**) vs single peaks from DFT in (**b**), see the main text and spectra shown in Figs. S8, S10, and S12.

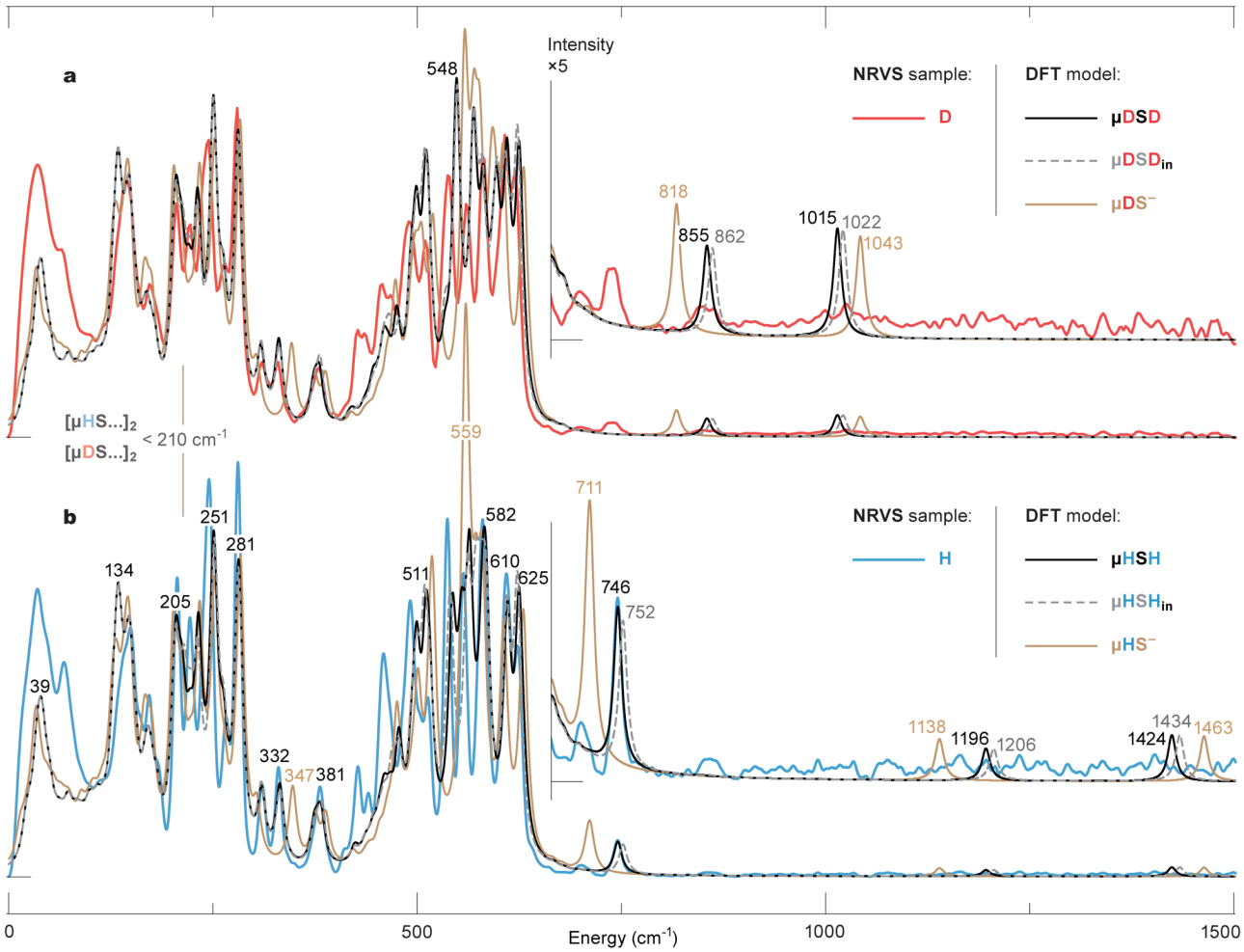

Fig. S8 Overlays of ^{57}Fe-PVDOS spectra for the (**b**) H- and (**a**) D-isotopologues of the **μHSH** compound from NRVS experiment (blue and red) and DFT modeling (black). The DFT spectra are additionally provided for the **μHSH$_{in}$** (grey, broken) and **μHS$^-$** (brown) alternative models shown in Fig. S3a. The bands from DFT are labeled with their positions (cm^{-1}); the corresponding normal mode animations for the **μHSH** and **μDSD** models are available in ESI† separately. The DFT intensities <210 cm^{-1} are based on the corresponding dimer calculations, as explained in the main text and shown in Fig. 5.

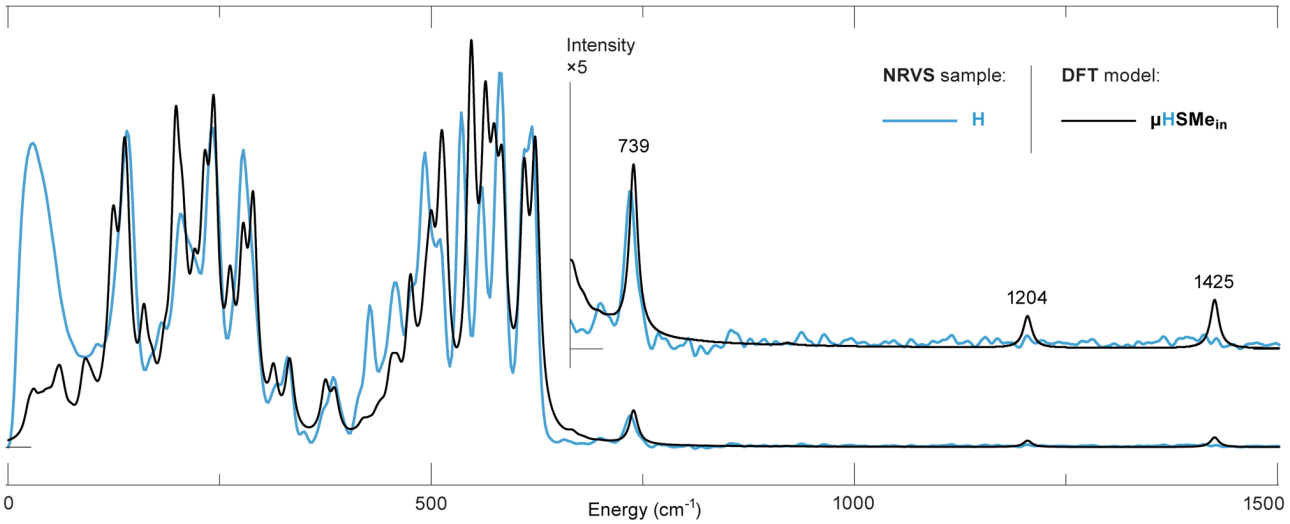

Fig. S9 Overlays of ^{57}Fe-PVDOS spectra for the H-isotopologue of the methylated **μHSMe$_{in}$** species (shown in Fig. S4) from NRVS experiment (blue) and DFT modeling (black). Important bands from DFT are labeled with their positions (cm^{-1}).

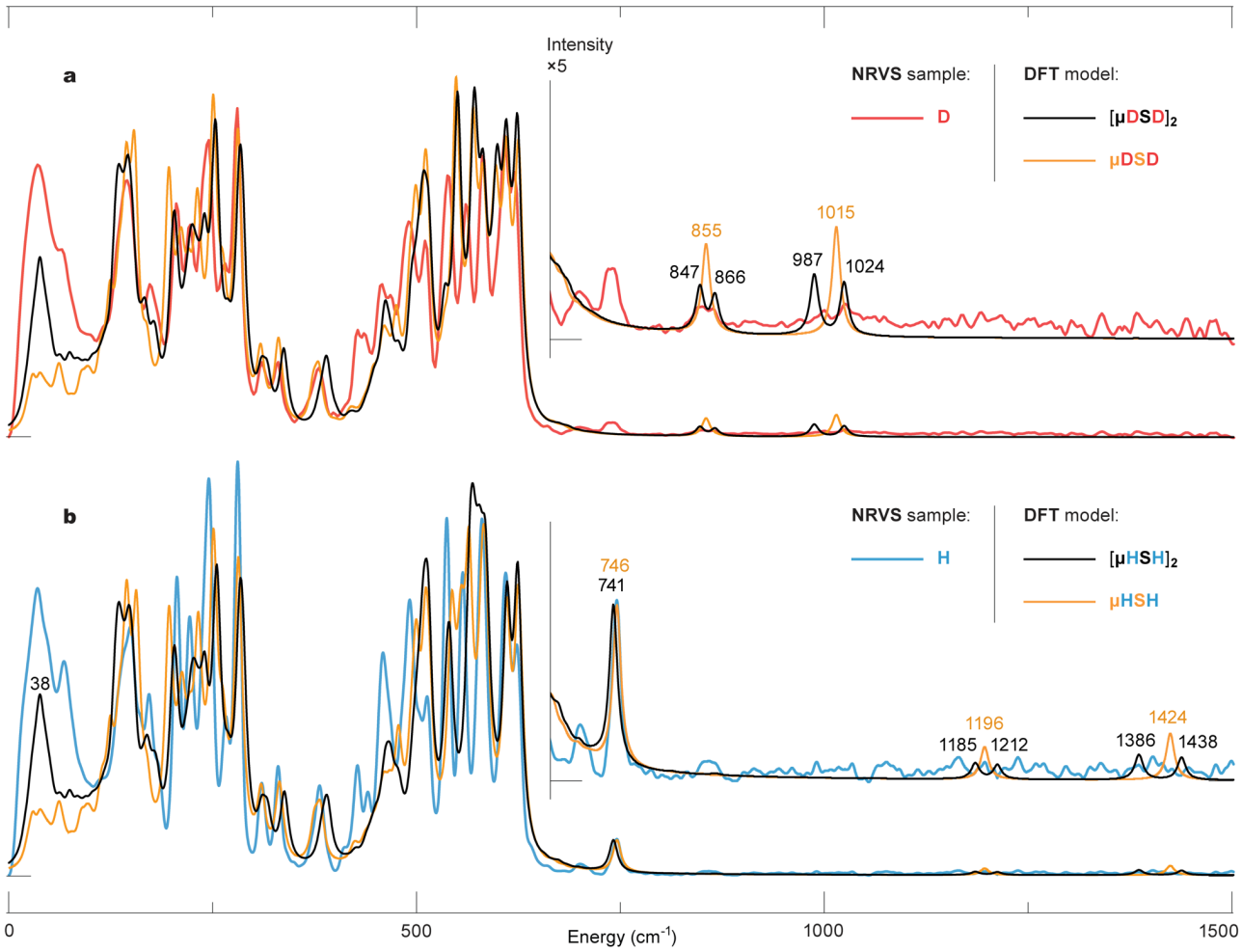

Fig. S10 Overlays of ^{57}Fe-PVDOS spectra for the (**b**) H- and (**a**) D-isotopologues of the **μHSH** compound from NRVS experiment (blue and red) and DFT modeling. The DFT spectra are shown for the monomer **μHSH** (orange, structure in Fig. S3a) and dimer **[μHSH]$_2$** (black, structure in Fig. S3b) models. Important bands from DFT are labeled with their positions (cm^{-1}); animated normal modes associated with these bands are available in ESI† separately.

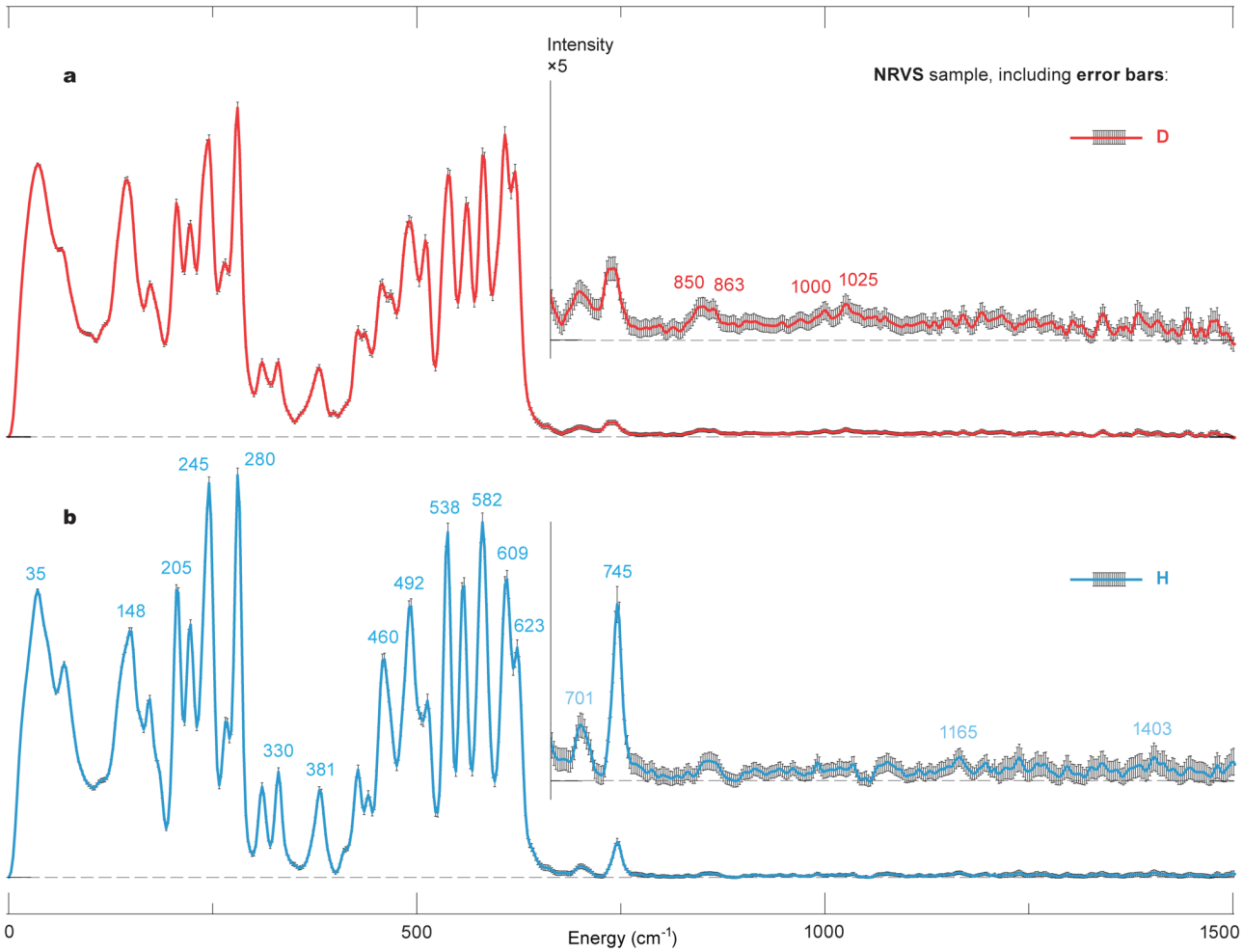

Fig. S11 ^{57}Fe-PVDOS spectra for the (**b**) H- (blue) and (**a**) D- (red) isotopologues of the **μHSH** compound from the NRVS experiment including the error bars (grey). The ×5 intensity insets display the 'active window' ^{57}Fe-hydride bands region >650 cm^{-1}. The observed NRVS bands are labeled with their positions (cm^{-1}); the assignments >800 cm^{-1} are tentative.

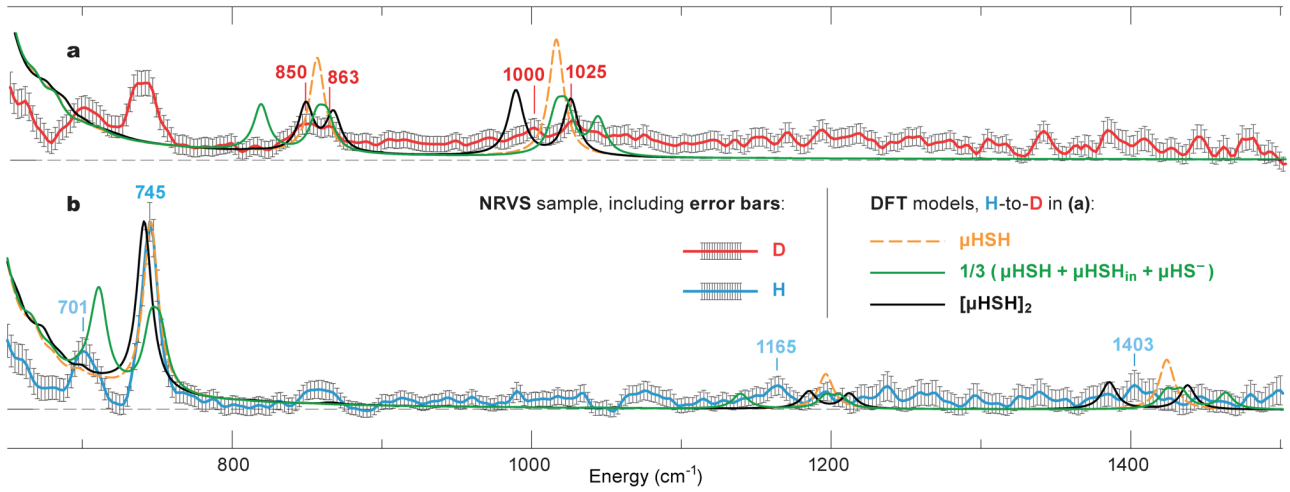

Fig. S12 ^{57}Fe-PVDOS spectra for the (**b**) H- (blue) and (**a**) D- (red) isotopologues of **μHSH** from the NRVS experiment including the error bars (grey) in the iron-hydride bands region >650 cm^{-1}, overlaid with the DFT spectra of the (*i*) **μHSH** monomer (orange, broken), (*ii*) averaged between the three **μHSH**/**μHSH$_{in}$**/**μHSH^{-}** monomers (green), and (*iii*) the **[μHSH]$_2$** dimer (black) models. The observed NRVS bands are labeled with their positions (cm^{-1}); the assignments >800 cm^{-1} are tentative.

References

1. P. Chernev, C. Lambertz, A. Brünje, N. Leidel, K. G. V. Sigfridsson, R. Kositzki, C.-H. Hsieh, S. Yao, R. Schiwon, M. Driess, C. Limberg, T. Happe and M. Haumann, *Inorg. Chem.*, 2014, **53**, 12164-12177.
2. S. Mebs, J. Duan, F. Wittkamp, S. T. Stripp, T. Happe, U.-P. Apfel, M. Winkler and M. Haumann, *Inorg. Chem.*, 2019, **58**, 4000-4013.
3. S. Mebs, M. Senger, J. Duan, F. Wittkamp, U.-P. Apfel, T. Happe, M. Winkler, S. T. Stripp and M. Haumann, *J. Am. Chem. Soc.*, 2017, **139**, 12157-12160.
4. E. J. Lyon, I. P. Georgakaki, J. H. Reibenspies and M. Y. Darensbourg, *J. Am. Chem. Soc.*, 2001, **123**, 3268-3278.
5. J. A. Cabeza, M. A. Martínez-García, V. Riera, D. Ardura and S. García-Granda, *Organometallics*, 1998, **17**, 1471-1477.
6. K.-T. Chu, Y.-C. Liu, Y.-L. Huang, C.-H. Hsu, G.-H. Lee and M.-H. Chiang, *Chem. - Eur. J.*, 2015, **21**, 10978-10982.
7. M.-W. Chung, Y.-C. Liu, T.-H. Yen and M.-H. Chiang, *ChemElectroChem*, 2018, **5**, 20-24.
8. Y. Yoda, M. Yabashi, K. Izumi, X. W. Zhang, S. Kishimoto, S. Kitao, M. Seto, T. Mitsui, T. Harami, Y. Imai and S. Kikuta, *Nuclear Instruments & Methods in Physics Research Section a-Accelerators Spectrometers Detectors and Associated Equipment*, 2001, **467**, 715-718.
9. W. Sturhahn, *Hyperfine Interact.*, 2000, **125**, 149-172.
10. L. B. Gee, spectra.tools, https://spectra.tools/cgi-bin/controller.pl?body=NRVS_Tool, (accessed 2019, 2015-2019).
11. D. W. Johnson and J. C. H. Spence, *J. Phys. D: Appl. Phys.*, 1974, **7**, 771-780.
12. H. J. Lipkin, *Annals of Physics*, 1962, **18**, 182-197.
13. Z. Klencsár, *Hyperfine Interact.*, 2013, **217**, 117-126.
14. Y. C. Liu, K. T. Chu, R. L. Jhang, G. H. Lee and M. H. Chiang, *Chem. Commun.*, 2013, **49**, 4743-4745.
15. M. J. Frisch, G. W. Trucks, H. B. Schlegel, G. E. Scuseria, M. A. Robb, J. R. Cheeseman, G. Scalmani, V. Barone, B. Mennucci, G. A. Petersson, H. Nakatsuji, M. Caricato, X. Li, H. P. Hratchian, A. F. Izmaylov, J. Bloino, G. Zheng, J. L. Sonnenberg, M. Hada, M. Ehara, K. Toyota, R. Fukuda, J. Hasegawa, M. Ishida, T. Nakajima, Y. Honda, O. Kitao, H. Nakai, T. Vreven, J. A. Montgomery, Jr., J. E. Peralta, F. Ogliaro, M. Bearpark, J. J. Heyd, E. Brothers, K. N. Kudin, V. N. Staroverov, R. Kobayashi, J. Normand, K. Raghavachari, A. Rendell, J. C. Burant, S. S. Iyengar, J. Tomasi, M. Cossi, N. Rega, J. M. Millam, M. Klene, J. E. Knox, J. B. Cross, V. Bakken, C. Adamo, J. Jaramillo, R. Gomperts, R. E. Stratmann, O. Yazyev, A. J. Austin, R. Cammi, C. Pomelli, J. W. Ochterski, R. L. Martin, K. Morokuma, V. G. Zakrzewski, G. A. Voth, P. Salvador, J. J. Dannenberg, S. Dapprich, A. D. Daniels, Ö. Farkas, J. B. Foresman, J. V. Ortiz, J. Cioslowski and D. J. Fox, *Gaussian 09, Revision D.01, Gaussian Inc., Wallingford CT, 2009*.
16. *Jaguar, version 9.4, Schrodinger, Inc., New York, NY, 2016.*
17. A. D. Becke, *Phys. Rev. A*, 1988, **38**, 3098-3100.
18. J. P. Perdew, *Phys. Rev. B*, 1986, **33**, 8822-8824.
19. R. Krishnan, J. S. Binkley, R. Seeger and J. A. Pople, *J. Chem. Phys.*, 1980, **72**, 650-654.
20. A. D. McLean and G. S. Chandler, *J. Chem. Phys.*, 1980, **72**, 5639-5648.
21. V. Pelmenschikov, J. A. Birrell, C. C. Pham, N. Mishra, H. Wang, C. Sommer, E. Reijerse, C. P. Richers, K. Tamasaku, Y. Yoda, T. B. Rauchfuss, W. Lubitz and S. P. Cramer, *J. Am. Chem. Soc.*, 2017, **139**, 16894-16902.
22. V. Pelmenschikov, L. B. Gee, H. Wang, K. C. MacLeod, S. F. McWilliams, K. L. Skubi, S. P. Cramer and P. L. Holland, *Angew. Chem., Int. Ed.*, 2018, **130**, 9511-9515.
23. V. Pelmenschikov, Y. Guo, H. Wang, S. P. Cramer and D. A. Case, *Faraday Discuss.*, 2011, **148**, 409-420.
24. S. Grimme, J. Antony, S. Ehrlich and H. Krieg, *J. Chem. Phys.*, 2010, **132**, 154104.
25. L. Goerigk and S. Grimme, *Phys. Chem. Chem. Phys.*, 2011, **13**, 6670-6688.
26. Chemcraft, - *graphical software for visualization of quantum chemistry computations.* *https://www.chemcraftprog.com*.
27. F. Neese, *Wiley Interdisciplinary Reviews: Computational Molecular Science*, 2012, **2**, 73-78.
28. P. J. Stephens, F. J. Devlin, C. F. Chabalowski and M. J. Frisch, *J. Phys. Chem.*, 1994, **98**, 11623-11627.
29. A. D. Becke, *J. Chem. Phys.*, 1993, **98**, 5648-5652.
30. C. T. Lee, W. T. Yang and R. G. Parr, *Phys. Rev. B*, 1988, **37**, 785-789.
31. S. H. Vosko, L. Wilk and M. Nusair, *Can. J. Phys.*, 1980, **58**, 1200-1211.
32. D. W. Mulder, Y. Guo, M. W. Ratzloff and P. W. King, *J. Am. Chem. Soc.*, 2017, **139**, 83-86.
33. Z. Xiao, Z. Wei, L. Long, Y. Wang, D. J. Evans and X. Liu, *Dalton Trans.*, 2011, **40**, 4291-4299.
34. M. Razavet, S. C. Davies, D. L. Hughes, J. E. Barclay, D. J. Evans, S. A. Fairhurst, X. Liu and C. J. Pickett, *Dalton Trans.*, 2003, **32**, 586-595.
35. A. Kochem, E. Bill, F. Neese and M. van Gastel, *Chem. Commun.*, 2015, **51**, 2099-2102.
36. K. Weber, T. Weyhermüller, E. Bill, Ö. F. Erdem and W. Lubitz, *Inorg. Chem.*, 2015, **54**, 6928-6937.
37. R. Bjornsson and M. Buhl, *Dalton Trans.*, 2010, **39**, 5319-5324.
38. M. Römelt, S. Ye and F. Neese, *Inorg. Chem.*, 2009, **48**, 784-785.
39. W. Massa, *Crystal Structure Determination*, Springer, New York, 2nd edn., 2000.